Applied Geochemistry 178 (2025) 106239

Contents lists available at ScienceDirect

Applied Geochemistry

journal homepage: www.elsevier.com/locate/apgeochem

Rare earth element (REE) speciation in municipal solid waste incineration ash

Yinghao Wen[a,1], Lei Hu[a,1], Pan Liu[a], Qian Wang[a], Estefania Garcia[a], Weiyao Yan[b], Yuanzhi Tang[a,*]

[a] *School of Earth and Atmospheric Sciences, Georgia Institute of Technology, 311 Ferst Drive, Atlanta, GA, 30332, United States*
[b] *Department of Earth and Atmospheric Sciences, University of Houston, 3507 Cullen Boulevard, Houston, TX, 77204, United States*

ARTICLE INFO

Editorial Handling by: Zimeng Wang

Keywords:
Rare earth elements
Municipal solid waste incineration ash
Synchrotron X-ray absorption spectroscopy
Synchrotron X-ray microscopy
Resource recovery

ABSTRACT

A robust and sustainable supply of rare earth elements (REE) is critically needed for clean-energy technologies, which has stimulated substantial interests in REE recovery from waste streams. Municipal solid waste incineration ash (MSWIA) was recently recognized as a potentially important REE resource, yet REE speciation in MSWIA remains poorly understood. This study employed synchrotron X-ray spectroscopy and microscopy techniques to elucidate the speciation of representative REE (Y, Ce, and Nd) in different MSWIA samples. Linear combination fitting of bulk X-ray absorption near edge structure (XANES) data indicated that Y-bearing Al/Fe oxides and phosphates are the primary Y-hosting phases. Micro-XANES of individual Y-containing particles identified by micro X-ray fluorescence (μXRF) mapping revealed notably different Y speciation at micro-scale from the bulk, consistent with the highly heterogeneous nature of MSWIA samples. The main REE-bearing phases in different size-fractionated MSWIA are similar: Y and Nd as oxides and xenotime/monazite, and Ce as apatite and monazite. Our results provide important insights for designing pre-screening processes (e.g., density separation) and optimizing extraction methods (e.g., pH, use of ligands) for cost-effective REE recovery from MSWIA.

1. Introduction

Rare earth elements (REE) play a pivotal role in global energy transition due to their irreplaceable roles in many clean energy technologies (Geng et al., 2023; Jowitt et al., 2018; Li et al., 2020; Prommer, 2023). For example, Nd and Pr are indispensable in permanent magnets used in wind turbines and electric vehicles. Manufacturing of high-temperature superconductors requires Gd and Eu. The global demand for REE is projected to increase five-fold from ~60,000 tons in 2005 to ~315,000 tons in 2030, yet the supply chain has been the “lagging strand” due to environmental considerations (Alonso et al., 2012; Li et al., 2020; Tukker, 2014). On average, producing one ton of purified REE from raw ores generates 9600–12,000 m^3 of toxic gas containing flue dust concentrate, HF, SO_2, and H_2SO_4, 200 m^3 of acid mine drainage containing heavy metals (e.g., Pb and Cd) and radioactive wastes (e.g., U and Th), and 2000 tons of solid residue (Lee and Wen, 2017; Navarro and Zhao, 2014; Paul and Campbell, 2011). In contrast, recycling REE from waste streams has the potential to strengthen REE supply while eliminating pollution at the same time. Technoeconomic and life cycle analysis suggested that REE recycling features a lower chemical/energy demand and lighter environmental impact compared to mining (Li et al., 2019; Sanchez Moran et al., 2024). The European Commission has passed a law that mandates 15% of REE consumption in the European Union to be covered by recycling by 2030 (Geng et al., 2023).

Municipal solid waste (MSW) contains energy-rich materials such as food wastes, wood-derived products, plastics, as well as many valuable metals including Cu, Mn, Zn, and REE (Beikmohammadi et al., 2023; Setoodeh Jahromy et al., 2019; Vergara and Tchobanoglous, 2012). MSW had a massive global production of 2.2 billion tons in 2020, and this number was projected to increase to 3.9 billion tons by 2050 (Vergara and Tchobanoglous, 2012). Due to environmental concerns associated with direct landfill, incineration of MSW in waste-to-energy (WTE) facilities has become a more appealing option (Mukherjee

---

* Corresponding author.
E-mail address: yuanzhi.tang@eas.gatech.edu (Y. Tang).
[1] Y.W. and L.H. contributed equally to this paper.

https://doi.org/10.1016/j.apgeochem.2024.106239
Received 24 August 2024; Received in revised form 21 October 2024; Accepted 26 November 2024

et al., 2020). This process produces municipal solid waste incineration ash (MSWIA) as the solid residual, with up to 90% reduction in volume/mass and generates electricity from heat (Jung et al., 2004; Scarlat et al., 2019). Fly ash is the fraction of MSWIA collected by air pollution controls (~20 wt%), and bottom ash comprises incombustible phases (~80 wt%) (Clavier et al., 2020; Mukherjee et al., 2020). While repurposing of MSWIA (e.g., as substitution materials in asphalt pavement and Portland cement) is commonly practiced in many countries with space constraints, over 95% of MSWIA produced in the U.S. is disposed of in landfills, posing potential risks of pollution (Clavier et al., 2019; Magnuson et al., 2023; Sarmiento et al., 2019; Wang et al., 2022). It has been previously overlooked that the volume/mass reduction during MSW incineration can enrich the total REE concentration to ~100–400 ppm in MSWIA, which is comparable to other REE-containing wastes (e.g., coal fly ash (Liu et al., 2023), spent magnets (Ding et al., 2022), phosphogypsum (Cánovas et al., 2019), and mine tailings (Ayora et al., 2016)). Note that the REE concentration in these secondary feedstocks is markedly lower than that in hard rock ores (>30,000 ppm) and ion adsorption clays (500–10,000 ppm) used in mining (Dushyantha et al., 2020). Nevertheless, REE recovery could be a promising alternative to supplement the primary production from mining, considering the massive and continuous production of these wastes (Allegrini et al., 2014; Funari et al., 2016).

However, major knowledge gaps need to be filled before feasible technologies can be developed for REE recovery from MSWIA. Characterizations of MSWIA in the literatures were mostly limited to mineralogy and REE concentrations in bulk samples, with very little information on the chemical speciation of REE (Allegrini et al., 2014; Burlakovs et al., 2018; Yao et al., 2014). REE can mainly exist in the natural environments as REE-oxides, bastnäsite [$(Ce,La)CO_3F$], monazite [$(Ce,La,Nd)PO_4$], and xenotime (YPO_4), or as trace phases in iron oxyhydroxides, apatite, zircon, glass, and organics (Stuckman et al., 2018). The extractability of REE is heavily governed by the solubility of REE-bearing phases and leaching chemistry. Dissolution of these phases is facilitated under acidic conditions and occurs at different pH ranges: REE-oxides and REE-carbonates at pH < 5.5, REE-apatites at pH < 3.5, REE-phosphates at pH < 1.5 (Liu et al., 2019; Stoy et al., 2021). Besides pH, certain organic ligands can enhance REE dissolution by forming REE-ligand complexes (Wen et al., 2024). A systematic understanding of the primary REE speciation in MSWIA can facilitate the design of efficient recovery technologies. In addition, determining the characteristics of REE in different size fractioned MSWIA particles is crucial from an engineering perspective. However, efforts have not been made in these regards, and such knowledge gaps need to be addressed.

In this study, we employed synchrotron X-ray spectroscopy and microscopy to characterize the REE speciation in MSWIA. Since MSWIA compositions are highly variable due to the lack of established MSW presorting in the U.S., we acquired 8 MSWIA samples from three WTE facilities from different geographic regions to account for different feedstock compositions and incineration conditions. One MSWIA sample representative with the highest total REE concentration was size-fractionated and characterized. X-ray absorption near edge structure (XANES) spectra of bulk MSWIA samples were collected to analyze the average REE speciation in the bulk phase. Micro X-ray fluorescence (μXRF) microscopy was conducted to identify the distribution and elemental association of REE-containing particles, accompanied with micro-XANES (μXANES) analysis for REE-speciation at micro-scale. Y was selected as the probe for heavy REE (HREE) and the major representative for all REE because: (1) the K-edge of Y has a characteristic XANES feature with little interference, and (2) the local coordination of Y often closely resembles that of other HREE such as Dy, Ho, and Yb (Elzinga et al., 2002; Kolker et al., 2017; Liu et al., 2019; Taggart et al., 2018; Tanaka et al., 2008). Ce and Nd were selected to represent light REE (LREE) because of their relatively high concentrations in our samples (Table 1) (Stuckman et al., 2018).

Combining spectroscopic and microscopic data allowed us to retrieve unique information on REE distribution and speciation. The oxidation states of REE and major REE-bearing phases in MSWIA were elucidated by fitting XANES spectra with reference compounds using linear combination fitting (LCF). The XANES spectra of REE collected at both the macro and micro scales provided valuable information on the heterogeneity and variability of REE-bearing phases in MSWIA. Together, these results could help fill up the current knowledge gap in understanding the speciation and extractability of REE in MSWIA and contribute to improving current REE recovery technologies.

Table 1
Weight percentages of major oxides and REE concentrations in MSWIA samples measured by ICP-MS and ICP-OES after microwave digestion (particle size: 2 mm; BDL: below detection limit of 1.0 ng/g).

Sample	C1 (Bottom ash)	C2 (Bottom ash)	C3 (Bottom ash)	C4 (Bottom ash)	S1 (Fly ash)	S2 (Bottom ash)	E1 (Combined ash)	E2 (Combined ash)
Major oxides (wt%)								
SiO_2	34.5 ± 1.4	35.0 ± 1.7	33.5 ± 1.2	30.5 ± 0.8	7.3 ± 0.5	34.2 ± 1.2	27.6 ± 1.1	21.0 ± 0.8
Al_2O_3	10.1 ± 0.6	9.0 ± 0.4	9.8 ± 0.8	9.9 ± 0.6	2.8 ± 0.3	15.8 ± 0.8	9.6 ± 0.7	9.2 ± 0.5
Fe_2O_3	9.9 ± 0.6	12.3 ± 0.5	10.3 ± 0.7	10.2 ± 0.7	0.9 ± 0.2	12.9 ± 0.4	8.2 ± 0.7	5.7 ± 0.4
CaO	19.2 ± 0.8	18.7 ± 1.1	17.9 ± 0.5	18.9 ± 0.3	41.9 ± 1.0	15.0 ± 0.4	15.5 ± 0.8	24.0 ± 1.2
REE (mg/kg)								
Sc	5.41 ± 0.31	5.63 ± 0.45	4.98 ± 0.53	3.23 ± 0.27	1.18 ± 0.25	4.65 ± 0.77	4.06 ± 0.66	3.62 ± 0.74
Y	17.02 ± 1.21	14.04 ± 0.78	10.26 ± 0.64	41.32 ± 1.64	4.52 ± 0.67	16.10 ± 0.94	13.46 ± 0.75	21.02 ± 1.71
La	17.75 ± 1.02	15.19 ± 1.20	17.91 ± 1.32	15.67 ± 1.44	5.75 ± 0.45	28.88 ± 1.43	21.72 ± 1.22	15.89 ± 0.88
Ce	37.81 ± 1.57	33.58 ± 1.44	27.53 ± 1.58	34.07 ± 1.03	9.83 ± 0.77	70.92 ± 2.18	45.19 ± 2.31	30.95 ± 1.33
Pr	5.17 ± 0.28	3.24 ± 0.37	2.90 ± 0.11	2.97 ± 0.54	0.89 ± 0.13	12.09 ± 0.58	4.38 ± 0.64	2.74 ± 0.31
Nd	13.45 ± 0.65	11.30 ± 0.14	11.24 ± 0.86	11.97 ± 0.88	3.52 ± 0.28	44.23 ± 1.38	17.11 ± 0.95	11.01 ± 0.74
Sm	3.80 ± 0.22	2.81 ± 0.03	1.78 ± 0.08	1.70 ± 0.43	0.51 ± 0.14	3.37 ± 0.11	2.32 ± 0.13	1.74 ± 0.24
Eu	2.34 ± 0.08	1.13 ± 0.05	0.62 ± 0.07	0.49 ± 0.07	0.11 ± 0.09	0.85 ± 0.13	0.51 ± 0.08	1.12 ± 0.33
Gd	3.51 ± 0.06	2.03 ± 0.07	1.51 ± 0.12	1.49 ± 0.11	0.40 ± 0.14	2.96 ± 0.74	2.15 ± 0.17	1.63 ± 0.28
Tb	2.17 ± 0.11	0.76 ± 0.07	0.30 ± 0.07	0.23 ± 0.03	BDL	0.28 ± 0.05	BDL	0.44 ± 0.12
Dy	3.38 ± 0.15	2.02 ± 0.10	1.42 ± 0.14	1.28 ± 0.14	0.39 ± 0.08	3.95 ± 0.14	1.92 ± 0.23	1.35 ± 0.18
Ho	1.97 ± 0.03	0.59 ± 0.04	0.22 ± 0.04	BDL	BDL	0.30 ± 0.04	BDL	BDL
Er	3.05 ± 0.05	1.72 ± 0.12	1.48 ± 0.55	0.97 ± 0.11	0.12 ± 0.05	1.78 ± 0.22	1.04 ± 0.08	0.72 ± 0.27
Tm	1.70 ± 0.03	0.38 ± 0.06	BDL	BDL	BDL	BDL	BDL	BDL
Yb	3.53 ± 0.08	1.22 ± 0.11	0.82 ± 0.06	0.83 ± 0.09	0.20 ± 0.06	1.32 ± 0.17	0.89 ± 0.09	0.65 ± 0.17
Lu	8.17 ± 0.12	0.50 ± 0.07	0.52 ± 0.05	1.43 ± 0.12	0.48 ± 0.05	BDL	BDL	BDL
ΣREE	130.24 ± 7.58	96.13 ± 6.12	83.51 ± 5.57	117.64 ± 7.12	27.90 ± 3.15	191.76 ± 9.89	114.99 ± 8.56	92.91 ± 8.31

2. Experimental section

2.1. Municipal solid waste incineration ash (MSWIA) samples

A total of 8 MSWIA samples were provided by three WTE facilities in the U.S. (two in the northeast and one in the northwest) and were labeled as C1, C2, C3, C4, S1, S2, E1, and E2. The as-received MSWIA samples were size fractionated using a standard testing sieve with a pore size of 2 mm, and the samples with a particle size of ≤2 mm (~60 wt%) were used in this study. Prior to characterizations, MSWIA sample was ground to fine powders using a pestle and mortar. The morphology and mineralogy of MSWIA samples were examined using scanning electron microscopy-energy dispersive spectroscopy (SEM-EDS) and X-ray diffraction (XRD). The elemental concentrations in the samples were measured using inductively coupled plasma-mass spectrometry (ICP-MS) and ICP-optical emission spectrometry (ICP-OES) after microwave digestion (**Supporting Information Text S1**). The S2 sample was further size-fractionated using standard testing sieves with size openings of 600 μm and 100 μm and then analyzed for REE concentrations and speciation.

2.2. Analytical methods

Details for SEM and XRD are described in Text S2. For synchrotron X-ray absorption spectroscopy (XAS) and microscopy analysis, Y was selected as the REE representative. Y K-edge bulk XANES of all MSWIA samples (particle size < 2 mm) and reference compounds were collected at Beamline 12-BM and 5-BM-D at Advanced Photon Source (APS), Argonne National Laboratory (Lemont, IL). Bulk XANES spectra of Ce and Nd L_{III}-edge were not collected due to interference from other metals (e.g., Ti and Ba) (Li et al., 2023). Finely ground samples were dusted onto Kapton tapes. $Y_2(CO_3)_3$ was used for energy alignment (17056.5 eV). Multiple scans (4–6) were collected for each sample. The spectra of reference compounds were collected using the same settings.

μXRF mapping of selected hotspots and μXANES spectra of Y K-edge, Ce L_{III}-edge, and Nd L_{III}-edge were collected at Beamline 13-ID-E at APS. Selected areas were mapped with a spatial resolution of 5 μm × 5 μm and a dwell time of 100 ms. $Y_2(CO_3)_3$ was used for energy alignment (17056.5 eV). $Ce_2(CO_3)_3$ and $Nd_2(CO_3)_3$ were used for energy alignment at 5726.5 eV for Ce L_{III}-edge and 6725.5 eV for Nd L_{III}-edge, respectively. μXANES spectra of selected Y hotspots were collected to determine micro-scale REE speciation. Due to the inference from other elements at Ce and Nd L_{III}-edges and the common co-occurrence of rare earth elements, the strategy was to collect XRF maps above Y K-edge, identify Y hot spots as candidate particles, then collect two smaller maps above and below Ce or Nd L_{III}-edge around the candidate particles. The subtracted data from these two maps represent the distribution of "true" Ce/Nd-containing particles and were used for μXANES analysis.

In order to identify and quantify the REE speciation in MSWIA samples, LCF analyses were conducted by fitting the XANES spectra of samples with those of reference compounds using the software Athena. Reference compounds of Y, Ce, and Nd are described in Table S1. The Y K-edge, Ce L_{III}-edge, and Nd L_{III}-edge XANES spectra of reference compounds are shown in Figs. S1–S3. One limitation of LCF is that the fitting results is affected by the selection of reference compounds and the results may not reflect the actual chemical speciation of the sample if certain phases are missing in the reference compounds. To address this limitation, we selected an inclusive set of reference compounds based on our understanding of MSWIA, common REE-bearing phases in geological samples, and thermally-stable REE-bearing phases in incineration byproducts from literatures (Liu et al., 2019, 2020; Stuckman et al., 2018; Taggart et al., 2018). Details of the reference compounds are in Table S1, including: dissolved REE (Y^{3+}, Ce^{3+}, Nd^{3+}), REE oxides (Y_2O_3, CeO_2, and Nd_2O_3), REE carbonates (Y-tengerite, Nd-tengerite, cerium carbonate, bastnäsite), REE phosphates (Y-churchite, xenotime, monazite, Nd-rhabdophane), REE-containing phosphors (Eu-doped Y_2O_3, Y–Al garnet, Y–Fe garnet), REE-bearing hematite, REE-bearing calcite, REE-organic complex (REE-lignin, REE-chitosan), REE-bearing glass phase, REE-bearing apatite, and REE-bearing zircon. Note that Eu-doped Y_2O_3 and two Y-doped garnets were included as reference compounds because they are commonly found in spent phosphors and could be a major REE source in MSW (Hossain et al., 2021; Liu et al., 2019; Taggart et al., 2018; Tan et al., 2015).

The fitting energy range for both bulk and micro XANES was from −30 eV to +150 eV. All weights of reference compounds were set to be within 0–1, but the sum of weights was not forced to be 1. E0 was allowed to float. The maximum number of reference compounds involved in LCF for each XANES spectrum was limited to 4. Fits were selected to minimize the *R*-factor and the number of reference compounds involved. The XANES spectra were first fitted using two reference compounds. Then a third reference compound was introduced to the fitting combination and was kept in the LCF results only if it: (1) reduced the *R*-factor by at least 10% and (2) accounted for at least 5% of total weight. A forth reference compound was then introduced and analyzed following the same procedure. The fitting results with the lowest *R*-factor were reported.

3. Results and discussion

3.1. Elemental composition of MSWIA

Sample C1–C4 (bottom ash) and E1–E2 (combined ash) have a similar ΣREE concentration ranging between ~90 and 130 mg/kg, whereas the ΣREE concentrations in S1 (fly ash) and S2 (bottom ash) are drastically different at 27.9 and 191.8 mg/kg, respectively (Table 1). The enrichment of REE in S2 bottom ash can be attributed to the low volatility of REE (Funari et al., 2016; Morf et al., 2013). Sample S2 with the highest ΣREE concentration among all samples was further size-fractionated into three fractions: 600 μm to 2 mm, 100–600 μm, and below 100 μm (hereafter denoted as 2 mm, 600 μm, and 100 μm sample, respectively). Interestingly, the ΣREE concentration was markedly enriched from the 2 mm fraction to the 100 μm fraction (Table S2), agreeing well with a previous study (Ma et al., 2019). The particularly high REE concentration in sample S2, especially Ce, Pr, and Nd, could be due to high content of electronic wastes in the raw MSW. Besides REE, the MSWIA samples are also abundant in many other elements such as Si, Ca, Fe, Al, and Mg (Table S3). Note that owing to the low Si content (<35 wt%), MSWIA could be more acid-soluble than other Si-rich REE-containing feedstocks such as Class-F coal fly ash and thus more feasible for recovery (e.g., does not require alkaline pretreatment to dissolve zircon/glass phases) (Liu et al., 2023; Wen et al., 2023).

3.2. Morphology and mineralogy of MSWIA

SEM images show that the particle size of MSWIA ranges from several microns to ~1–2 mm (Figs. S4–S5). MSWIA particles covers a variety of morphology, including spherical, near-cubic shaped, and irregularly shaped particles and clusters. Some smaller particles appear to be welded on the surface of larger particles, likely as a result of particle agglomeration at high incineration temperatures (Chang and Wey, 2006). Based on the XRD patterns, the major crystalline phases in the MSWIA samples are quartz and calcium magnesium aluminum silicate, with some minor fractions of halite, hematite, and calcite (Fig. S6). Although the typical incineration temperature of MSW in the U.S. (~990–1100 °C) is above the decomposition temperature of calcite, short retention time of MSW during incineration (~1–2 s) might result in incomplete decomposition (Giraud et al., 2021). The presence of several unidentified peaks could be attributed to the complex matrix of MSWIA and varying incineration procedures/conditions of different WTE facilities.

3.3. Y speciation in MSWIA – bulk XANES

The Y K-edge XANES spectra of reference compounds are shown in Fig. S1, which display four types of spectral features. A strong single-peak spectrum at ~17056 eV is observed for Y^{3+} (aq), Y-doped iron garnet ($Y_3Fe_5O_{12}$), Y-tengerite [$Y_2(CO_3)_3 \cdot 2–3H_2O$], bastnäsite [(Ce, La, Nd)CO_3(F,OH)], Y-bearing hematite (Fe_2O_3), and REE-organic complexes (chitosan and lignin). A strong peak followed by a weak shoulder hump at ~17066 eV is observed for Y-doped aluminum garnet (YAG, $Y_3Al_5O_{12}$), churchite ($YPO_4 \cdot 2H_2O$), monazite [(Ce, Th, La, Nd)PO_4], xenotime [(Y, Dy)PO_4], and Y-bearing zircon ($ZrSiO_4$). A weak peak followed by a shoulder hump is observed for Y-oxide (Y_2O_3), Eu-doped Y_2O_3 ($Y_{1.92}Eu_{0.08}O_3$), Y-bearing apatite [$Ca_5(PO_4)_3$(F,Cl,OH)], and Y-bearing glass. In addition, Y-bearing calcite ($CaCO_3$) shows a unique dual-peak spectrum. The difference in spectral features of these reference compounds reflects different local coordination environment of Y in these phases.

To determine the bulk Y speciation in MSWIA, LCF was performed on the bulk XANES spectra of the MSWIA samples using the reference compounds (Fig. 1a). Initially, LCF was performed without including the three reference compounds for spent phosphors (Table S4). The LCF results indicate the primary presence of Y as 26.4–93.1% Y-bearing oxides (Y_2O_3 and hematite) and 5.3–73.7% Y-phosphates (apatite and xenotime) in all samples. The *R*-factor of LCF ranges from 0.00255 to 0.0054, except for sample S1, which has a markedly higher value due to high signal noise. Surprisingly, Y-lignin as an unstable phase at high temperature accounts for ~11.5–30.0% of Y speciation in most of MSWIA samples.

On the other hand, the LCF results that include the Y-containing phosphors are shown in Fig. 1 and Table 2. The updated fitting results suggest that Y predominantly exist as Y-bearing Al/Fe oxides ($Y_3Al_5O_{12}$ and hematite) and Y-phosphates (apatite and xenotime), in which $Y_3Al_5O_{12}$ completely replaces Y_2O_3 and Y-organics. Samples C1–C4 exhibit very similar profiles, with $Y_3Al_5O_{12}$ (22.5–50.4%) and hematite (33.8–56.2%) together accounting for over 75% of Y speciation, and the remaining fraction is apatite (15.9–24.5%). Samples E1–E2 show a higher fraction of Y-bearing hematite (47.5–72.5%), and about 10.9–35.1% of Y as xenotime instead of apatite. Sample S1 as the only fly ash representative contains Y mostly as apatite (74.5%), whereas sample S2 as the bottom ash from the same WTE facility comprises 44.5% of Y as xenotime, 41.4% as $Y_3Al_5O_{12}$, and 13.9% as hematite. For sample S1–S2, inclusion of Y-containing phosphors notably improves the *R*-factor by ~22–42% and thus reflects the Y speciation more accurately (Table 2 vs. Table S4). Note that Y-bearing hematite is the only reference compound in Table 2 that displays a single-peak spectrum at ~17056 eV, whereas the other three all have a single peak followed by a weak shoulder hump at ~17066 eV (Fig. S1). As a result, the spectra of samples S1 and S2 with the lowest fraction of Y-bearing hematite (<14%) exhibit an obvious shoulder hump, and those of sample C2 and E1 with the highest fraction of hematite (>56%) show a clear single-peak feature (Fig. 1a).

Table 2
LCF results of Y K-edge bulk XANES (particle size: 2 mm; LCF-derived errors are shown in parentheses).

Bulk sample	Y species (%)				*R*-factor
	Y-bearing Al/Fe oxides		Y-phosphates		
	YAG ($Y_3Al_5O_{12}$)	Hematite	Apatite	Xenotime	
C1	28.4 (7.7)	51.8 (11.2)	19.8 (5.1)	–	0.00447
C2	22.5 (5.8)	56.2 (7.4)	21.4 (6.5)	–	0.00276
C3	38.9 (7.5)	36.5 (8.8)	24.5 (6.6)	–	0.00421
C4	50.4 (6.3)	33.8 (5.9)	15.9 (4.3)	–	0.00312
S1	15.7 (7.6)	9.9 (5.7)	74.5 (11.2)		0.01423
S2	41.4 (8.9)	13.9 (6.9)	–	44.5 (7.4)	0.00422
E1	16.5 (3.7)	72.5 (8.8)	–	10.9 (5.1)	0.00241
E2	17.5 (8.4)	47.5 (8.5)	–	35.1 (9.6)	0.00367

Although the difference in *R*-factor of sample C1–C4 and E1–E2 with and without including Y-containing phosphors is mathematically indistinguishable (≤10%), the updated fitting results that included phosphors are more reasonable. The absence of thermally unstable Y-organic complexes could be attributed to decomposition during MSW incineration (~990–1100 °C) to form oxides and phosphates, which are stable phases at temperature up to 1500 °C (Giraud et al., 2021; Liu et al., 2020). Previous speciation studies on coal ash did not consider REE-containing phosphors because they are irrelevant, but we included them in this study because of their potential presence in unsorted MSW (Hossain et al., 2021; Liu et al., 2019; Taggart et al., 2018).

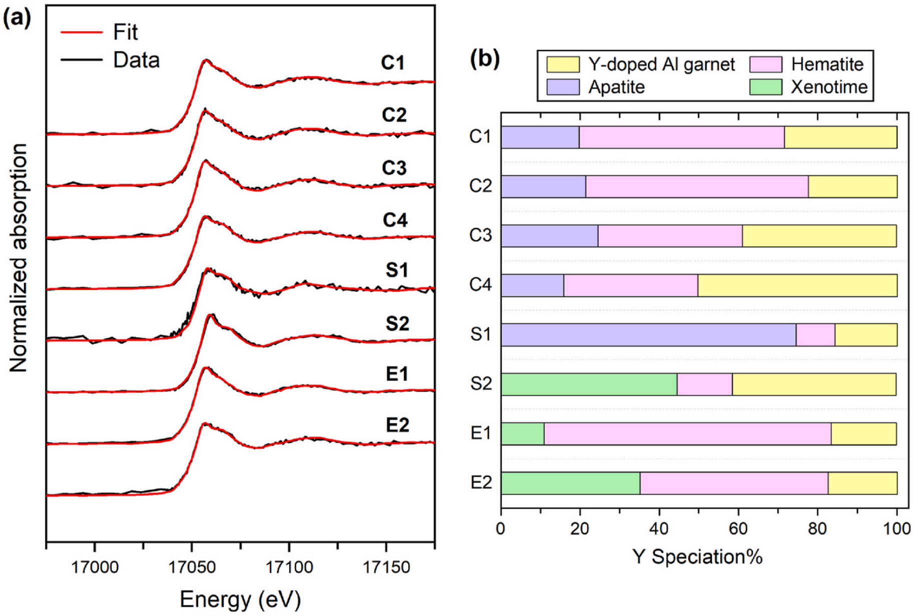

Fig. 1. **(a)** Normalized spectra of Y K-edge bulk XANES (black lines) of the MSWIA samples (particle size: 2 mm) and fitted LCF curves (red lines); **(b)** corresponding Y speciation with the lowest *R*-factor determined by LCF.

3.4. Micro-scale Y speciation in MSWIA – µXRF and µXANES

As the average Y speciation at the bulk scale is revealed by bulk XANES, µXRF mapping followed by µXANES were also performed to elucidate REE speciation at the micro-scale and correlation with other elements. Sample C1 and C4 were selected because of their high Y concentration (Table 1). According to the LCF results of bulk XANES, the main Y speciation in sample C1 includes 51.8% hematite, 28.4% YAG, and 19.8% apatite, whereas sample C4 contains 50.4% YAG, 33.8% hematite, and 15.9% apatite (Table 2).

Representative µXRF maps of selected hotspots are shown in Fig. 2. The two Y hotspots in sample C1 (C1_1 and C1_2) have a size of ~10 µm (Fig. 2a-b). Hotspot C1_1 is co-localized with Nd, Eu, and P, but not with Fe. The µXANES spectrum of C1_1 shows a weak peak followed by a shoulder hump, which closely resembles that of Y_2O_3 (Fig. 3a, Fig. S1). As expected, the LCF results indicate that Y predominantly exists as 86.6% Y_2O_3 (Fig. 3b, Table 3), which could be formed via decomposition of Y-organics or Y-carbonates during incineration (Liu et al., 2020). The co-localization of Y with P can be attributed to 13.4% of Y as apatite, and the absence of Fe-containing phases is also consistent with the µXRF map. The µXRF maps of C1_2 show the co-localization of Y with Ce, Nd, Eu, and Fe. The presence of 43.1% Y as YAG and 30.4% as xenotime in C1_2 gives it a distinct feature with a strong peak followed by a weak shoulder hump (Table 3). The co-localization of Y with Fe can be ascribed to 26.4% of Y as hematite. Based on LCF results and the µXRF map, hotspot C1_2 is likely a small YAG/xenotime particle fused with a bigger LREE-bearing hematite particle.

For sample C4, hotspot C4_1 has a size of ~10 µm, whereas C4_2 is smaller at ~5 µm (Fig. 2c-d). Co-localization of Y with other LREE (e.g., Ce, Nd, and Eu) is observed on both hotspots. The µXANES spectra of C4_1 and C4_2 exhibit a similar feature as that of C1_1, as they all contain a significant fraction of Y as Y_2O_3 (68.7% in C4_1 and 84.3% in C4_2) (Fig. 3, Table 3). The co-localization of Y with Fe in C4_1 can be attributed to 24.2% of Y as hematite, while the concurrence of Y and P in C4_2 is likely due to Y-bearing xenotime. Hotspot C4_2 could be an Y_2O_3 particle fused with a piece of REE-bearing phosphate mineral that can accommodate light-to-medium REE (e.g., monazite).

Interestingly, the composition of Y-bearing phases in all examined hotspots are not completely the same as the bulk XANES results (Table 3). This implies the significant heterogeneity of Y distribution in MSWIA, in which the average Y speciation determined by bulk XANES might not represent the local speciation of individual particles. On the other hand, while µXRF/µXANES can reveal REE distribution and identify REE-bearing phases at the micro-scale, the representativeness of results is limited by the randomness of hotspot selection (Liu et al., 2019). Hence, bulk XANES and µXRF/µXANES complement each other at the bulk and micro-scale to help us obtain a comprehensive understanding of REE speciation in MSWIA. We also point out that despite the difference in results, the major Y speciation at the macro- and micro-scales can be categorized into similar phase groups: ~70–87% Y-bearing (Al/Fe) oxides and ~13–30% Y-bearing phosphates for sample C1; ~84–90% Y-bearing (Al/Fe) oxides and ~10–16% Y-bearing phosphates for sample C4 (Table 3).

3.5. Micro-scale speciation of Y, Ce, and Nd in size-fractionated MSWIA

Since it has been reported that many metals can partition into different particle sizes of MSWIA (Allegrini et al., 2014;

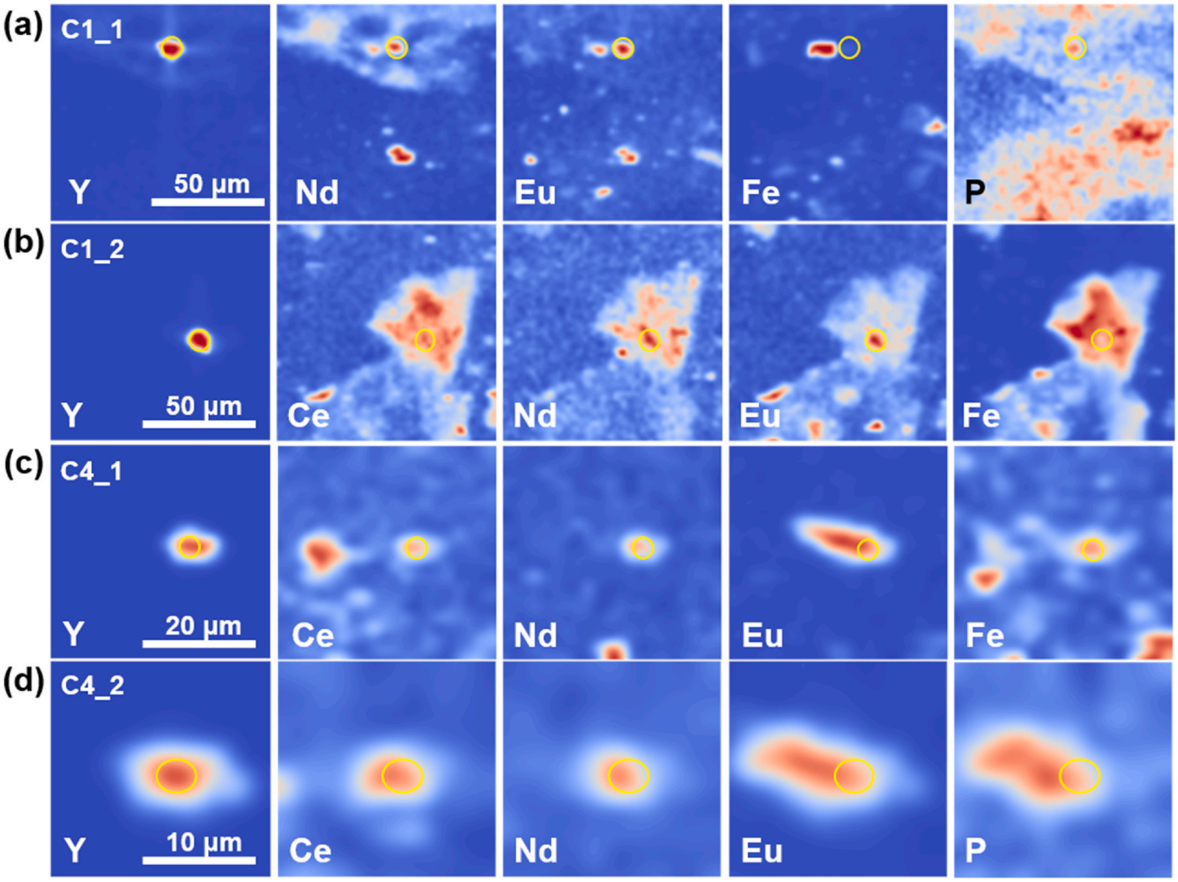

Fig. 2. Representative µXRF maps of selected REE and other elements in hotspots of C1 and C4 samples. **(a)** Y, Nd, Eu, Fe, and P maps in hotspot 1 of sample C-1; (b) Y, Ce, Nd, Eu, and Fe maps in hotspot 2 of sample C1; (c) Y, Ce, Nd, Eu, and Fe maps in hotspot 1 of sample C4; (d) Y, Ce, Nd, Eu, and P maps in hotspot 2 of sample C4. The hotspots are indicated by yellow circles and selected for µXANES analysis (shown in Fig. 3).

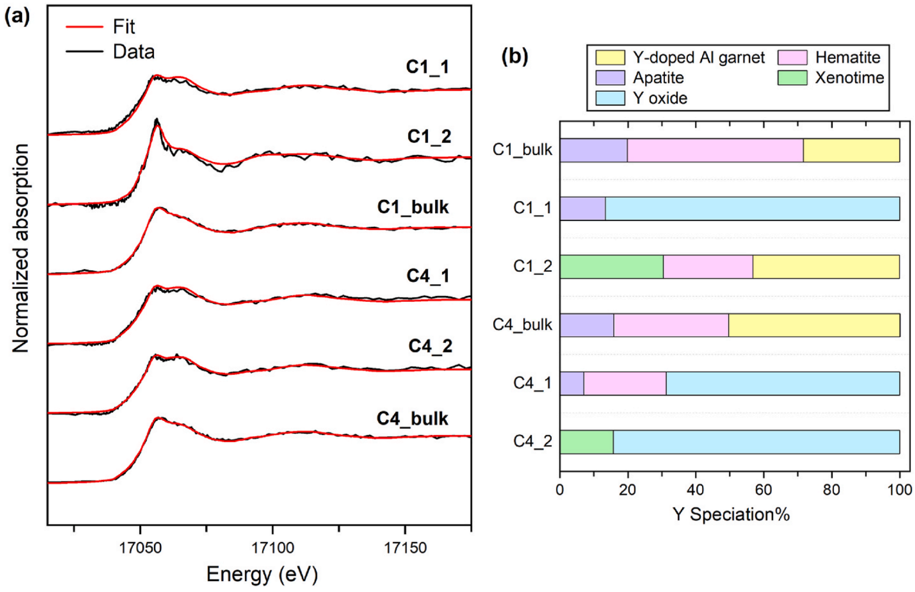

Fig. 3. **(a)** Normalized spectra of Y K-edge bulk XANES of sample C1 and C4, μXANES of selected hotspots (black lines), and fitted LCF curves (red lines); **(b)** corresponding Y speciation with the lowest *R*-factor determined by LCF.

Table 3
LCF results of Y K-edge bulk- and μXANES spectra for sample C1 and C4 (particle size: 2 mm; LCF derived errors are shown in parentheses).

Bulk samples and hotspots	Y species (%)					*R*-factor
	Y-bearing (Al/Fe) oxides			Y-phosphates		
	Y_2O_3	YAG ($Y_3Al_5O_{12}$)	Hematite	Apatite	Xenotime	
C1_bulk	–	28.4 (7.7)	51.8 (11.2)	19.8 (5.1)	–	0.00447
C1_1 spot	86.6 (6.5)	–	–	13.4 (6.2)	–	0.01241
C1_2 spot	–	43.1 (7.8)	26.4 (8.2)	–	30.4 (10.5)	0.01127
C4_bulk	–	50.4 (6.3)	33.8 (5.9)	15.9 (4.3)	–	0.00312
C4_1 spot	68.7 (5.9)	–	24.2 (10.1)	7.1 (5.5)	–	0.01021
C4_2 spot	84.3 (4.5)	–	–	–	15.7 (4.4)	0.00425

Beikmohammadi et al., 2023; Morf et al., 2013), sample S2 with a particularly high ΣREE concentration was further size-fractionated into three groups as mentioned earlier and analyzed for REE speciation using μXRF/μXANES. Ce and Nd were also analyzed as LREE representatives besides Y. The XANES spectrum of Ce L_{III}-edge displays distinctive features depending on the oxidation state (Takahashi et al., 2002). Most of the Ce reference compounds used in this study contain Ce(III), and their L_{III}-edge XANES spectra show a clear single-peak at ~5726.5 eV, whereas Ce(IV)-containing reference compounds (e.g. CeO_2) have dual-peaks at ~5731.9 and ~5738.4 eV (Fig. S2). On the other hand, the Nd L_{III}-edge XANES spectra of all reference compounds are very similar, with a strong absorption peak at ~6725.5 eV and a broad hump at ~6756.3 eV. Due to the lack of distinctive spectral difference in the XANES spectra, identifying Ce and Nd speciation solely based on LCF can be difficult, and thus combining LCF with μXRF maps can provide more insights.

In the 100 μm size-fractionated S2 sample, two hotspots were selected for each of Y, Ce, and Nd to determine their correlation with other elements. Hotspots S2-100_Y_1 and S2-100_Y_2 have a spherical shape and a particle size of ~7–8 μm (Figs. S7a–b). Both hotspots are co-present with Eu and P, but not with Ce. The μXANES spectrum of S2-100_Y_1 shows a strong shoulder hump at ~17066 eV following the peak at ~17056 eV, which can be ascribed to the dominant presence of Y_2O_3 (89.4%) as suggested by LCF results (Fig. 4a, Table 4). The minor correlation of Y with P is likely due to apatite as a trace phase. The μXANES spectrum of S2-100_Y_2 has a strong peak followed by a weak shoulder hump, and the major presence of xenotime (64.0%) is revealed by LCF results (Fig. 4a), which also agrees well with the stronger correlation of Y with P compared to S2-100_Y_1 (Table 4, Figs. S7a–b).

According to the μXRF maps, both Ce hotspots show a clear correlation with Nd, Pr, and P (Figs. S7c–d). Hotspot S2-100_Ce_1 has a crescent shape that seems to be on the edge of a larger spherical particle with a diameter of >100 μm, whereas hotspot S2-100_Ce_2 is a small spherical particle of ~10 μm. The μXANES spectra of both hotspots display a single peak feature at ~5726.5 eV, suggesting that Ce primarily exists as Ce^{3+} (Fig. 4b). LCF results reveal that Ce is present as a mixture of apatite and monazite, which matches well with the co-presence of Ce with other LREE and the strong correlation with P. Similarly, apparent correlation of Nd with Ce and Pr is also observed in both Nd hotspots and confirmed by LCF results that monazite accounts for ~87–90% of Nd speciation (Fig. 4c, Figs. S7e–f, Table 4). The co-presence of Nd with Ca is likely due to apatite as a trace phase (~11–14%).

For the 600 μm size-fractionated S2 sample, distinctive speciation was observed in the two selected Y hotspots. In S2-600_Y_1, Y clearly co-exists with Eu and Ce, while in S2-600_Y_2, Y shows no correlation with them (Figs. S8a–b). The XANES spectrum of S2-600_Y_1 has a weak peak followed by a shoulder hump, whereas the spectrum of S2-600_Y_2 has a strong peak followed by a shoulder hump (Fig. 4d). The LCF results indicate 91.2% of Y in S2-600_Y_1 as Y_2O_3 and 86.5% of Y in S2-600_Y_2 as xenotime (Table 4). On the other hand, μXRF maps of Ce and Nd suggest the co-occurrence of Ce, Pr, and Nd in all selected particles (Figs. S8c–f). LREE-bearing monazite is identified as the main hosting phase in these hotspots, accounting for ~67–96% of Ce and ~44–64% of Nd, whereas the remaining fractions of Ce and Nd likely exist as REE-bearing apatite and Nd_2O_3, respectively (Table 4).

For the 2 mm size-fractionated S2 sample, co-occurrence of different REE in selected particles was observed in μXRF maps (Fig. S9). For example, Y was found to co-present with several LREE (e.g., Eu and Ce) in Y hotspots (Figs. S9a–b). The LCF results indicate that xenotime and Y_2O_3 constitute over 80% of Y speciation (Table 4). Similarly to the S2-

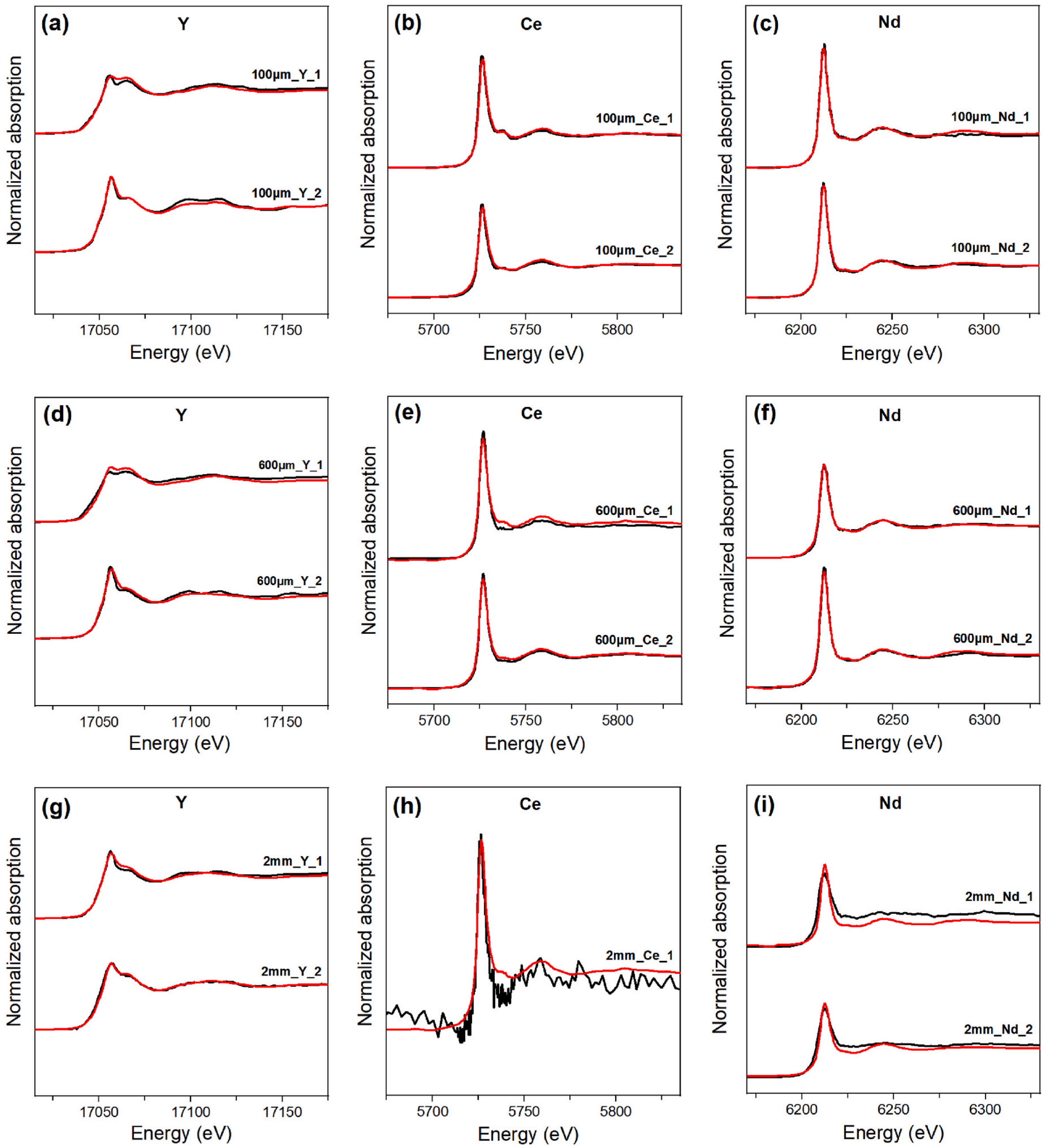

Fig. 4. Normalized spectra of Y K-edge, Ce L_{III}-edge, and Nd L_{III}-edge μXANES of hotspots identified by μXRF maps for **(a–c)** 100 μm, **(d–f)** 600 μm, and **(g–i)** 2 mm size-fractionated S2 samples (black lines). Corresponding LCF results are shown in red lines.

600 μm sample, concurrent presence of Ce, Pr, and Nd was also observed in the S2-2 mm sample (Figs. S9c–e). As expected, the majority of Ce and Nd exists as LREE-bearing monazite. Nd_2O_3 is another major host of Nd (up to 45%), and REE-bearing apatite likely hosts the remaining ~15–24% of Ce and Nd (Table 4).

Even though enrichment in REE concentration in smaller-sized MSWIA was observed, the major speciation of REE representatives in these size-fractionated samples does not show any significant difference based on μXRF/μXANES. Y is primarily present as xenotime and Y_2O_3, Ce mainly exists as monazite and apatite, and Nd is mostly found in monazite and Nd_2O_3. Compared to bulk XANES, μXANES suggests markedly different Y speciation in S2 samples, especially the absence of YAG (Table 2 vs. Table 4). As discussed earlier, this is likely due to sample heterogeneity and randomness of hotspot selection using μXRF.

4. Conclusion

This study systematically investigated the chemical speciation of Y, Ce, and Nd in different MSWIA samples using XAS techniques. LCF results of bulk XANES indicate the dominant presence of Y as Y-bearing Al/Fe oxides (YAG and hematite) and Y-phosphates (apatite and xenotime), which are chemically and thermally stable phases remained after MSW incineration. Importantly, YAG constitutes ~15–50% of Y speciation in all MSWIA samples, inferring that MSW contains a substantial amount of spent phosphors as a major REE source. In addition, μXRF maps elucidate the strong correlation between Y and other elements (e.g., Fe and P), matching well with μXANES results. Clear heterogeneity was also observed, in which the average Y speciation suggested by bulk XANES is different from that by μXANES. To obtain a comprehensive understanding of REE speciation, complementary XAS

Table 4
LCF results of Y K-edge, Ce L_{III}-edge, and Nd L_{III}-edge µXANES for the 100 µm, 600 µm, and 2 mm size-fractionated S2 samples (LCF-derived errors are shown in parentheses).

Y	Y species (%)				*R*-factor
	Y-bearing (Fe) oxides		Y-phosphates		
	Y_2O_3	Hematite	Apatite	Xenotime	
S2-100_Y_1	89.4 (5.2)	–	10.6 (5.0)	–	0.00815
S2-100_Y_2	8.3 (2.4)	27.7 (6.5)	–	64.0 (7.0)	0.00288
S2-600_Y_1	91.2 (7.7)	–	–	9.1 (2.7)	0.00924
S2-600_Y_2	13.6 (1.4)	–	–	86.5 (3.7)	0.00743
S2-2_Y_1	21.9 (4.4)	–	18.5 (4.8)	59.6 (3.0)	0.00475
S2-2_Y_1	48.3 (4.8)	–	–	51.7 (4.4)	0.00196

Ce	Ce species (%)		*R*-factor
	Ce-phosphates		
	Apatite	Monazite	
S2-100_Ce_1	46.8 (3.6)	53.3 (3.9)	0.00475
S2-100_Ce_2	72.3 (3.9)	27.7 (6.3)	0.00718
S2-600_Ce_1	32.9 (8.8)	67.1 (13.8)	0.04776
S2-600_Ce_2	3.8 (1.0)	96.2 (3.4)	0.00836
S2-2_Ce_1	23.9 (13.2)	76.0 (11.4)	0.01041

Nd	Nd species (%)			*R*-factor
	Nd-oxide	Nd-phosphates		
	Nd_2O_3	Apatite	Monazite	
S2-100_Nd_1	–	10.5 (5.1)	89.5 (5.4)	0.00376
S2-100_Nd_2	–	13.5 (3.8)	86.5 (3.9)	0.00198
S2-600_Nd_1	35.6 (1.9)	–	64.4 (2.2)	0.00325
S2-600_Nd_2	56.2 (6.2)	–	43.8 (5.9)	0.00393
S2-2_Nd_1	45.1 (18.1)	14.7 (2.1)	40.3 (15.3)	0.10431
S2-2_Nd_1	8.6 (2.7)	–	91.6 (13.1)	0.00924

analyses at both bulk and micro-scale are necessary. Furthermore, despite the REE enrichment in finer MSWIA particles, the major REE speciation in 2 mm, 600 µm, and 100 µm fractionated samples is consistent. Y and Nd mainly exist as REE-oxides (Y_2O_3 and Nd_2O_3) and REE-phosphates (xenotime and monazite), whereas Ce is primarily present as monazite or apatite.

Our findings have important implications for REE recovery from MSWIA, as it has been recognized as an emerging REE resource. Elucidating the dominant REE speciation in MSWIA produced by different WTE facilities can help us design and optimize extraction methods for REE recovery based on the solubility/reactivity of these REE-bearing phases under different leaching conditions (Liu et al., 2019; Stoy et al., 2021). Unlike in some coal ashes (Taggart et al., 2018), REE in MSWIA samples are not found in acid-resistant phases (e.g., glass, zircon, and silicates), and thus energy- and chemical-intensive alkaline pretreatment is not needed to liberate encapsulated REE phases. REE-bearing oxides and phosphates can be readily dissolved at $pH > 1$ and even under less acidic conditions in the presence of certain ligands (e.g., citrate) (Liu et al., 2019; Wen et al., 2023; Wen et al., 2024). In addition, density-based screening processes such as dense medium separation can be designed to separate REE-bearing phases from gangues prior to extraction, which can drastically reduce the feedstock volume.

CRediT authorship contribution statement

Yinghao Wen: Writing – review & editing, Writing – original draft, Visualization, Validation, Investigation, Formal analysis. **Lei Hu:** Writing – review & editing, Investigation. **Pan Liu:** Writing – review & editing, Investigation. **Qian Wang:** Writing – review & editing, Investigation. **Estefania Garcia:** Writing – review & editing, Investigation. **Weiyao Yan:** Writing – review & editing, Investigation. **Yuanzhi Tang:** Writing – review & editing, Supervision, Resources, Project administration, Methodology, Investigation, Funding acquisition, Conceptualization.

Declaration of competing interest

The authors declare that they have no known competing financial interests or personal relationships that could have appeared to influence the work reported in this paper.

Acknowledgements

This work was supported by the Department of Energy ARPA-E Grant #DE-AR0001394 and National Science Foundation Grant # 2327660. We thank the beamline scientists at beamlines 5-BM-D, 12-BM-B and 13 ID-E of the Advanced Photon Source (APS) for their support with experimental set up and data collection. APS is a U.S. Department of Energy (DOE) Office of Science User Facility operated for the DOE Office of Science by Argonne National Laboratory under Contract No. DE-AC02-06CH11357. A portion of the analyses was performed at the Georgia Tech Institute for Electronics and Nanotechnology (IEN), a member of the National Nanotechnology Coordinated Infrastructure (NNCI) supported by the National Science Foundation (Grant ECCS-2025462).

Appendix A. Supplementary data

Supplementary data to this article can be found online at https://doi.org/10.1016/j.apgeochem.2024.106239.

Data availability

Data will be made available on request.

References

Allegrini, E., Maresca, A., Olsson, M.E., Holtze, M.S., Boldrin, A., Astrup, T.F., 2014. Quantification of the resource recovery potential of municipal solid waste incineration bottom ashes. Waste Manag. 34, 1627–1636. https://doi.org/10.1016/j.wasman.2014.05.003.

Alonso, E., Sherman, A.M., Wallington, T.J., Everson, M.P., Field, F.R., Roth, R., Kirchain, R.E., 2012. Evaluating rare earth element availability: a case with revolutionary demand from clean technologies. Environ. Sci. Technol. 46, 3406–3414. https://doi.org/10.1021/es203518d.

Ayora, C., Macías, F., Torres, E., Lozano, A., Carrero, S., Nieto, J.-M., Pérez-López, R., Fernández-Martínez, A., Castillo-Michel, H., 2016. Recovery of rare earth elements and yttrium from passive-remediation systems of acid mine drainage. Environ. Sci. Technol. 50, 8255–8262. https://doi.org/10.1021/acs.est.6b02084.

Beikmohammadi, M., Yaghmaeian, K., Nabizadeh, R., Mahvi, A.H., 2023. Analysis of heavy metal, rare, precious, and metallic element content in bottom ash from municipal solid waste incineration in Tehran based on particle size. Sci. Rep. 13, 16044. https://doi.org/10.1038/s41598-023-43139-1.

Burlakovs, J., Jani, Y., Kriipsalu, M., Vincevica-Gaile, Z., Kaczala, F., Celma, G., Ozola, R., Rozina, L., Rudovica, V., Hogland, M., 2018. On the way to 'zero waste'management: recovery potential of elements, including rare earth elements, from fine fraction of waste. J. Clean. Prod. 186, 81–90. https://doi.org/10.1016/j.jclepro.2018.03.102.

Cánovas, C., Chapron, S., Arrachart, G., Pellet-Rostaing, S., 2019. Leaching of rare earth elements (REEs) and impurities from phosphogypsum: a preliminary insight for further recovery of critical raw materials. J. Clean. Prod. 219, 225–235. https://doi.org/10.1016/j.jclepro.2019.02.104.

Chang, F.-Y., Wey, M.-Y., 2006. Comparison of the characteristics of bottom and fly ashes generated from various incineration processes. J. Hazard Mater. 138, 594–603. https://doi.org/10.1016/j.jhazmat.2006.05.099.

Clavier, K.A., Liu, Y., Intrakamhaeng, V., Townsend, T.G., 2019. Re-evaluating the TCLP's role as the regulatory driver in the management of municipal solid waste incinerator ash. Environ. Sci. Technol. 53, 7964–7973. https://doi.org/10.1021/acs.est.9b01370.

Clavier, K.A., Paris, J.M., Ferraro, C.C., Townsend, T.G., 2020. Opportunities and challenges associated with using municipal waste incineration ash as a raw ingredient in cement production–a review. Resour. Conserv. Recycl. 160, 104888. https://doi.org/10.1016/j.resconrec.2020.104888.

Ding, A., Liu, C., Zhang, X., Lei, L., Xiao, C., 2022. ZnCl$_2$: a green brønsted acid for selectively recovering rare earth elements from spent NdFeB permanent magnets. Environ. Sci. Technol. 56, 4404–4412. https://doi.org/10.1021/acs.est.1c08260.

Dushyantha, N., Batapola, N., Ilankoon, I., Rohitha, S., Premasiri, R., Abeysinghe, B., Ratnayake, N., Dissanayake, K., 2020. The story of rare earth elements (REEs): occurrences, global distribution, genesis, geology, mineralogy and global production. Ore Geol. Rev. 122, 103521. https://doi.org/10.1016/j.oregeorev.2020.103521.

Elzinga, E., Reeder, R., Withers, S., Peale, R.E., Mason, R., Beck, K.M., Hess, W.P., 2002. EXAFS study of rare-earth element coordination in calcite. Geochem. Cosmochim. Acta 66, 2875–2885. https://doi.org/10.1016/S0016-7037(02)00888-8.

Funari, V., Bokhari, S.N.H., Vigliotti, L., Meisel, T., Braga, R., 2016. The rare earth elements in municipal solid waste incinerators ash and promising tools for their prospecting. J. Hazard Mater. 301, 471–479. https://doi.org/10.1016/j.jhazmat.2015.09.015.

Geng, Y., Sarkis, J., Bleischwitz, R., 2023. How to build a circular economy for rare-earth elements. Nature 619, 248–251. https://doi.org/10.1038/d41586-023-02153-z.

Giraud, R.J., Taylor, P.H., Huang, C.-p., 2021. Combustion operating conditions for municipal Waste-to-Energy facilities in the US. Waste Manag. 132, 124–132. https://doi.org/10.1016/j.wasman.2021.07.015.

Hossain, M.K., Hossain, S., Ahmed, M.H., Khan, M.I., Haque, N., Raihan, G.A., 2021. A review on optical applications, prospects, and challenges of rare-earth oxides. ACS Appl. Electron. Mater. 3, 3715–3746. https://doi.org/10.1021/acsaelm.1c00682.

Jowitt, S.M., Werner, T.T., Weng, Z., Mudd, G.M., 2018. Recycling of the rare earth elements. Curr. Opin. Green Sustainable Chem. 13, 1–7. https://doi.org/10.1016/j.cogsc.2018.02.008.

Jung, C., Matsuto, T., Tanaka, N., Okada, T., 2004. Metal distribution in incineration residues of municipal solid waste (MSW) in Japan. Waste Manag. 24, 381–391. https://doi.org/10.1016/S0956-053X(03)00137-5.

Kolker, A., Scott, C., Hower, J.C., Vazquez, J.A., Lopano, C.L., Dai, S., 2017. Distribution of rare earth elements in coal combustion fly ash, determined by SHRIMP-RG ion microprobe. Int. J. Coal Geol. 184, 1–10. https://doi.org/10.1016/j.coal.2017.10.002.

Lee, J.C., Wen, Z., 2017. Rare earths from mines to metals: comparing environmental impacts from China's main production pathways. J. Ind. Ecol. 21, 1277–1290. https://doi.org/10.1111/jiec.12491.

Li, J., Peng, K., Wang, P., Zhang, N., Feng, K., Guan, D., Meng, J., Wei, W., Yang, Q., 2020. Critical rare-earth elements mismatch global wind-power ambitions. One Earth 3, 116–125. https://doi.org/10.1016/j.oneear.2020.06.009.

Li, W., Yamada, S., Hashimoto, T., Okumura, T., Hayakawa, R., Nitta, K., Sekizawa, O., Suga, H., Uruga, T., Ichinohe, Y., 2023. High-sensitive XANES analysis at Ce L$_2$-edge for Ce in bauxites using transition-edge sensors: implications for Ti-rich geological samples. Anal. Chim. Acta 1240, 340755. https://doi.org/10.1016/j.aca.2022.340755.

Li, Z., Diaz, L.A., Yang, Z., Jin, H., Lister, T.E., Vahidi, E., Zhao, F., 2019. Comparative life cycle analysis for value recovery of precious metals and rare earth elements from electronic waste. Resour. Conserv. Recycl. 149, 20–30. https://doi.org/10.1016/j.resconrec.2019.05.025.

Liu, P., Huang, R., Tang, Y., 2019. Comprehensive understandings of rare earth element (REE) speciation in coal fly ashes and implication for REE extractability. Environ. Sci. Technol. 53, 5369–5377. https://doi.org/10.1021/acs.est.9b00005.

Liu, P., Yang, L., Wang, Q., Wan, B., Ma, Q., Chen, H., Tang, Y., 2020. Speciation transformation of rare earth elements (REEs) during heating and implications for REE behaviors during coal combustion. Int. J. Coal Geol. 219, 103371. https://doi.org/10.1016/j.coal.2019.103371.

Liu, P., Zhao, S., Xie, N., Yang, L., Wang, Q., Wen, Y., Chen, H., Tang, Y., 2023. Green approach for rare earth element (REE) recovery from coal fly ash. Environ. Sci. Technol. 57, 5414–5423. https://doi.org/10.1021/acs.est.2c09273.

Ma, Z., Shan, X., Cheng, F., 2019. Distribution characteristics of valuable elements, Al, Li, and Ga, and rare earth elements in feed coal, fly ash, and bottom ash from a 300 MW circulating fluidized bed boiler. ACS Omega 4, 6854–6863. https://doi.org/10.1021/acsomega.9b00280.

Magnuson, J.K., Weiksnar, K.D., Patel, A.D., Clavier, K.A., Ferraro, C.C., Townsend, T.G., 2023. Processing municipal solid waste incineration bottom ash for integration into cement product manufacture. Resour. Conserv. Recycl. 198, 107139. https://doi.org/10.1016/j.resconrec.2023.107139.

Morf, L.S., Gloor, R., Haag, O., Haupt, M., Skutan, S., Di Lorenzo, F., Böni, D., 2013. Precious metals and rare earth elements in municipal solid waste–sources and fate in a Swiss incineration plant. Waste Manag. 33, 634–644. https://doi.org/10.1016/j.wasman.2012.09.010.

Mukherjee, C., Denney, J., Mbonimpa, E., Slagley, J., Bhowmik, R., 2020. A review on municipal solid waste-to-energy trends in the USA. Renew. Sustain. Energy Rev. 119, 109512. https://doi.org/10.1016/j.rser.2019.109512.

Navarro, J., Zhao, F., 2014. Life-cycle assessment of the production of rare-earth elements for energy applications: a review. Front. Energy Res. 2, 45. https://doi.org/10.3389/fenrg.2014.00045.

Paul, J., Campbell, G., 2011. Investigating rare earth element mine development in EPA region 8 and potential environmental impacts. A National Service Center for Environmental Publications 35.

Prommer, H., 2023. Towards sustainable rare-earth-element mining. Nat. Sustain. 6, 13–14. https://doi.org/10.1038/s41893-022-01014-3.

Sanchez Moran, E., Prodius, D., Nlebedim, I.C., Mba Wright, M., 2024. Rare-earth elements recovery from electronic waste: techno-economic and life cycle analysis. ACS Sustain. Chem. Eng. https://doi.org/10.1021/acssuschemeng.4c04100.

Sarmiento, L.M., Clavier, K.A., Paris, J.M., Ferraro, C.C., Townsend, T.G., 2019. Critical examination of recycled municipal solid waste incineration ash as a mineral source for portland cement manufacture–A case study. Resour. Conserv. Recycl. 148, 1–10. https://doi.org/10.1016/j.resconrec.2019.05.002.

Scarlat, N., Fahl, F., Dallemand, J.-F., 2019. Status and opportunities for energy recovery from municipal solid waste in Europe. Waste and Biomass Valorization 10, 2425–2444. https://doi.org/10.1007/s12649-018-0297-7.

Setoodeh Jahromy, S., Jordan, C., Azam, M., Werner, A., Harasek, M., Winter, F., 2019. Fly ash from municipal solid waste incineration as a potential thermochemical energy storage material. Energy Fuels 33, 5810–5819. https://doi.org/10.1021/acs.energyfuels.8b04106.

Stoy, L., Diaz, V., Huang, C.-H., 2021. Preferential recovery of rare-earth elements from coal fly ash using a recyclable ionic liquid. Environ. Sci. Technol. 55, 9209–9220. https://doi.org/10.1021/acs.est.1c00630.

Stuckman, M.Y., Lopano, C.L., Granite, E.J., 2018. Distribution and speciation of rare earth elements in coal combustion by-products via synchrotron microscopy and spectroscopy. Int. J. Coal Geol. 195, 125–138. https://doi.org/10.1016/j.coal.2018.06.001.

Taggart, R.K., Rivera, N.A., Levard, C., Ambrosi, J.-P., Borschneck, D., Hower, J.C., Hsu-Kim, H., 2018. Differences in bulk and microscale yttrium speciation in coal combustion fly ash. Environ. Sci. J. Integr. Environ. Res.: Process. Impacts 20, 1390–1403. https://doi.org/10.1039/c8em00264a.

Takahashi, Y., Sakami, H., Nomura, M., 2002. Determination of the oxidation state of cerium in rocks by Ce L$_{III}$-edge X-ray absorption near-edge structure spectroscopy. Anal. Chim. Acta 468, 345–354. https://doi.org/10.1016/S0003-2670(02)00709-2.

Tan, Q., Li, J., Zeng, X., 2015. Rare earth elements recovery from waste fluorescent lamps: a review. Crit. Rev. Environ. Sci. Technol. 45, 749–776. https://doi.org/10.1080/10643389.2014.900240.

Tanaka, K., Takahashi, Y., Shimizu, H., 2008. Local structure of Y and Ho in calcite and its relevance to Y fractionation from Ho in partitioning between calcite and aqueous solution. Chem. Geol. 248, 104–113. https://doi.org/10.1016/j.chemgeo.2007.11.003.

Tukker, A., 2014. Rare earth elements supply restrictions: market failures, not scarcity, hamper their current use in high-tech applications. Environ. Sci. Technol. 48, 9973–9974. https://doi.org/10.1021/es503548f.

Vergara, S.E., Tchobanoglous, G., 2012. Municipal solid waste and the environment: a global perspective. Annu. Rev. Environ. Resour. 37, 277–309. https://doi.org/10.1146/annurev-environ-050511-122532.

Wang, Y., Dong, J., Liu, J., Zheng, R., Yue, Y., Zhang, Y., Qian, G., 2022. Toward a sustainable municipal solid waste incineration fly-ash utilization network: integrating hybrid life cycle assessment with multiobjective optimization. ACS Sustain. Chem. Eng. 10, 7635–7647. https://doi.org/10.1021/acssuschemeng.2c01468.

Wen, Y., Hu, L., Boxleiter, A., Li, D., Tang, Y., 2023. Rare earth elements recovery and waste management of municipal solid waste incineration ash. ACS Sustainable Resource Management 1, 17–27. https://doi.org/10.1021/acssusresmgt.3c00026.

Wen, Y., Liu, P., Wang, Q., Zhao, S., Tang, Y., 2024. Organic ligand-mediated dissolution and fractionation of rare-earth elements (REEs) from carbonate and phosphate minerals. ACS Earth Space Chem. https://doi.org/10.1021/acsearthspacechem.4c00009.

Yao, Q., Samad, N.B., Keller, B., Seah, X.S., Huang, L., Lau, R., 2014. Mobility of heavy metals and rare earth elements in incineration bottom ash through particle size reduction. Chem. Eng. Sci. 118, 214–220. https://doi.org/10.1016/j.ces.2014.07.013.